Efficient estimation of personalized biventricular mechanical function employing gradient-based optimization

Henrik Finsberg, Ce Xi, Ju Le Tan, Liang Zhong, Martin Genet, Joakim Sundnes, Lik Chuan Lee, Samuel Wall

Received ; | Revised ; | Accepted

DOI: xxx/xxxx

ARTICLE TYPE

Efficient estimation of personalized biventricular mechanical function employing gradient-based optimization.

Henrik Finsberg[1,5,6] | Ce Xi[2] | Ju Le Tan[3] | Liang Zhong[3,4] | Martin Genet[8,9] | Joakim Sundnes[1,5,6] | Lik Chuan Lee[2] | Samuel T. Wall[1,5,7]

[1]Simula Research Laboratory, Oslo, Norway
[2]Department of Mechanical Engineering, Michigan State University, East Lansing, U.S.A
[3]National Heart Center Singapore, Singapore
[4]Duke National University of Singapore
[5]Center for Cardiological Innovation, Songsvannsveien 9, 0372 Oslo, Norway
[6]Department of Informatics, University of Oslo, P.O. Box 1080, Blindern 0316 Oslo, Norway
[7]Department of Mathematical Science and Technology, Norwegian University of Life Sciences, Universitetstunet 3 1430 Ås, Norway
[8]Mechanics Department and Solid Mechanics Laboratory, École Polytechnique (CNRS, Paris-Saclay University), Palaiseau, France
[9]M3DISIM research team, INRIA (Paris-Saclay University), Palaiseau, France

Correspondence
Henrik Finsberg, Simula Research Laboratory, P.O. Box 134, 1325 Lysaker Norway.
Email: henriknf@simula.no

Abstract

Individually personalized computational models of heart mechanics can be used to estimate important physiological and clinically-relevant quantities that are difficult, if not impossible, to directly measure in the beating heart. Here we present a novel and efficient framework for creating patient-specific biventricular models using a gradient-based data assimilation method for evaluating regional myocardial contractility and estimating myofiber stress. These simulations can be performed on a regular laptop in less than two hours and produce excellent fit between measured and simulated volume and strain data through the entire cardiac cycle. By applying the framework using data obtained from three healthy human bi-ventricles, we extracted clinically important quantities as well as explored the role of fiber angles on heart function. Our results show that steep fiber angles at the endocardium and epicardium are required to produced simulated motion compatible with measured strain and volume data. We also find that the contraction and subsequent systolic stresses in the right ventricle are signficantly lower than in the left ventricle. Variability of the estimated quantities with respect to both patient data and modeling choices are also found to be low. Because of its high efficiency, this framework may be applicable to modeling of patient specific cardiac mechanics for diagnostic purposes.

KEYWORDS:
Cardiac mechanics, Patient specific simulations, Parameter estimation, Data assimilation, Stress estimation, Contractility estimation

1 | INTRODUCTION

Cardiac computational modeling has emerged as both a powerful method to provide basic insight into cardiac function/ dysfunction, and as a support tool to improve current clinical practice. Its development is in part driven by significant advancements in medical imaging techniques (Pope et al. 2008; Townsend 2008; Lamata et al. 2014), which now provide a wealth of information about cardiac structure and kinematics. Merging this information with biophysical descriptions of cardiac behavior allows for the creation of powerful patient specific models of the heart (Krishnamurthy et al. 2013; Lee et al. 2014; Chabiniok et al. 2016). Such models can be used to predict the outcome of different treatment strategies (Sermesant et al. 2012) or to extract useful indicators of mechanical function, such as myocardial contractility (Chabiniok et al. 2012; Finsberg et al. 2017) and myofiber stress (Genet et al. 2014; Xi et al. 2016), potential biomarkers which are currently difficult, if not impossible, to measure directly using imaging techniques (Huisman et al. 1980).

Of particular importance is ventricular myofiber stress (Yin 1981), which is hypothesized to be a key driver of pathological remodeling processes in cardiac diseases (Grossman et al. 1975). Correspondingly, quantifying stress and determining how cardiac interventions may reduce abnormal

stress is considered a useful avenue in developing treatments for heart failure (Guccione et al. 2003). However, while measurements of heart motion are possible using an array of imaging techniques, no direct measurements of the load experienced by myocytes are currently possible in vivo and estimates are used instead. One widely used method is the law of Laplace, a simplified model that takes into account pressure, wall thickness and curvature, and can be used to evaluate stress in idealized geometries. However, despite its wide use, it has been shown that this law severely underestimates myofiber stress in largely irregular patient-specific ventricular geometries (Zhang et al. 2011). Furthermore, regional stresses also cannot be accurately estimated using this idealized law.

In order to overcome these limitations, patient specific simulation using finite element modeling is widely accepted as a viable way to accurately estimate myofiber stresses in the complex geometry of the heart, and has been used in designing heart failure treatments to reduce myocardial stress (Lee et al. 2013; Guccione et al. 2003; Wall et al. 2006). However, one of the many challenges faced by researchers developing patient specific models is to efficiently and accurately incorporate individual data into the them, which often requires determining model parameters that best reproduce the observations i.e., data assimilation (Sermesant et al. 2006; Chapelle et al. 2013). Typically, one defines a cost function representing the mismatch between simulated and observed data, and searches for model parameters that minimize this cost function. Several techniques have been employed to solve this minimization problem. Global methods, using parameter sweeps (Asner et al. 2015; Genet et al. 2015a; Xi et al. 2013) or genetic algorithms (Nair et al. 2007; Sun et al. 2009), are attractive because they can cover the entire parameter space, and are therefore more likely to retrieve the global mimumum of the cost function. However, such methods require an extensive number of functional evaluations, which in the case of heart mechanics can be computationally expensive. Local optimization methods, on the other hand, typically start at some given initial guess, and iteratively search the local neighborhood for better candidates in the minimization of the cost function. These methods are typically faster than global methods, but have the drawback that the solution may depend on the initial guess. One example of a local method is the reduced order unscented Kalman filtering (ruKF) approach (Moireau and Chapelle 2011), which has been applied to personalize cardiac electromechanical models from cine MRI (Marchesseau et al. 2013).

Another class of local optimization methods are the gradient-based methods, which successively reduce the cost functional by searching along the gradient descent direction. While these methods may substantially improve the convergence towards the minimum, estimating the gradient in these methods, however, introduces significant additional computational costs. Specifically, estimating the gradient by standard finite differences typically requires as many functional evaluations as the number of control parameters (N + 1 evaluations for N parameters). Gradient-based methods are therefore impractical if the number of control parameters is large. Nevertheless, gradient based approaches have been applied to personalize cardiac mechanics models in several studies (Balaban et al. 2016; Sermesant et al. 2006; Wang et al. 2009; Delingette et al. 2012). For example in (Wang et al. 2009) a sequential quadratic programming (SQP) optimization technique was utilized to estimate passive material parameters, while in (Göktepe et al. 2011) a Levenberg–Marquardt method was used to estimate material parameters from shear data. In (Delingette et al. 2012) the minimization was performed using a quasi-Newton BFGS-B method, where the gradient was computed using the adjoint method. In this study, however, the adjoint equation was derived analytically, which may be challenging in more complex problems of cardiac mechanics. More recently, a new approach based on automated derivation of functional gradients via solving the corresponding adjoint system have emerged (Farrell et al. 2013). Overcoming the issue that gradient-based methods face in dealing with a large number of parameters, this approach enables one to compute the functional gradient at a computational expense that does not depend on the number of control parameters (Balaban et al. 2016).

Here, we apply such a gradient-based data assimilation framework in order to fuse clinical imaging data from a cohort of healthy subjects to a biventricular mechanics model accurately and efficiently. By relating physical processes to the kinematics observed in medical images, we extracted clinically important quantities from these subject-fitted models and evaluated the sensitivity of these quantities to modeling choices such as fiber architecture and model for active contraction.

The paper is organized as follows. In Section 2 we present the pipeline for data assimilation, that includes an outline of the underlying ventricular mechanics model and solution methods. Section 3 presents the results of applying the framework to imaging data acquired from three healthy subjects, including a comparison of model prediction with the observed data, analysis of mechanical parameters extracted from the model, and a sensitivity analysis of model parameters to the input data. Finally, in sections 4 and 5 we discuss the performance of the framework and draw conclusions about its applicability in clinical settings.

2 | METHODS

2.1 | Data acquisition and pre-processing

Cine magnetic resonance (MR) images of 3 healthy subjects, referred here as CASE1, CASE2 and CASE3, were acquired at the National Heart Center of Singapore and written informed consent was obtained from all participants. Three-dimensional biventricular geometries of each subject were manually segmented from the MR images at multiple cardiac time points using the medical image analysis software MeVisLab (http://www.mevislab.de).

Cavity volumes of the left ventricle (LV) and right ventricle (RV) were computed from the segmented geometries at different time points in a cardiac cycle in each subject. Using a method described in (Xi et al. 2016), these volumes were paired with normal left and right ventricular pressure wave forms from previous studies (Redington et al. 1988) to construct pressure-volume loops of the LV and RV. Based on a previous empirical study (Kelly et al. 1992), LV pressure for each subject was also scaled so that the end-systolic pressure is 90% of the measured cuff pressure.

The observed regional circumferential and longitudinal Green-Lagrange strains in the LV free wall (LVFW), septum and RV free wall (RVFW) were estimated from the MR images in each subject using an hyperelastic warping technique (Veress et al. 2005; Genet et al. 2016). The output of this pre-processing step is used to calculate the estimated regional strain-time data. Briefly, a bi-ventricular finite element model reconstructed from the end-systolic (template) image was registered to all other cine (target) images acquired in the cardiac cycle by minimizing the squared difference between the target and template image intensities. This ill-posed correlation problem is regularized by also minimizing a prescribed (Neo-Hookean) strain energy function over the mesh. We note that other regularization approaches have also been proposed, such as regularization based on incompressibility (Mansi et al. 2011) or on equilibrium (Claire et al. 2004; Genet et al. 2017). Hyperelastic warping offers a good balance between regularization and strain estimation (Genet et al. 2016). The implementation of the image correlation procedure is based on FEniCS (Alnæs et al. 2015), and is freely available[1].

Three-dimensional biventricular meshes of the three normal subjects were created using Gmsh (Geuzaine and Remacle 2009) with the number of elements ranging from 4000 - 8000 tetrahedral elements. The chosen reference geometries were reconstructed from MR images in late diastole, and all meshes were uniformly refined in order to perform a convergence analysis .

Rule based fibers were assigned using the Laplace Dirichlet Rule-Based (LDRB) algorithm (Bayer et al. 2012). Although previous histological studies (Streeter et al. 1969) suggest that myofiber fiber helix angle varies transmurally from $+60^\circ$ at the endocardium to -60° at the epicardium, variability in fiber angle, nevertheless, exists between individuals. Therefore, we seek to also test how different fiber angle gradient alters the parameter estimation and the extracted outputs. More specifically, an angle $+\alpha/-\alpha$ is prescribed on the endo-/epicardium for α ranging from 30° to 80° at increments of 10°. If not otherwise specified, an angle of $+60^\circ$ and -60° on the endo- and epicardium respectively is prescribed. In Figure 1 we show this range of fiber fields for one of the subjects.

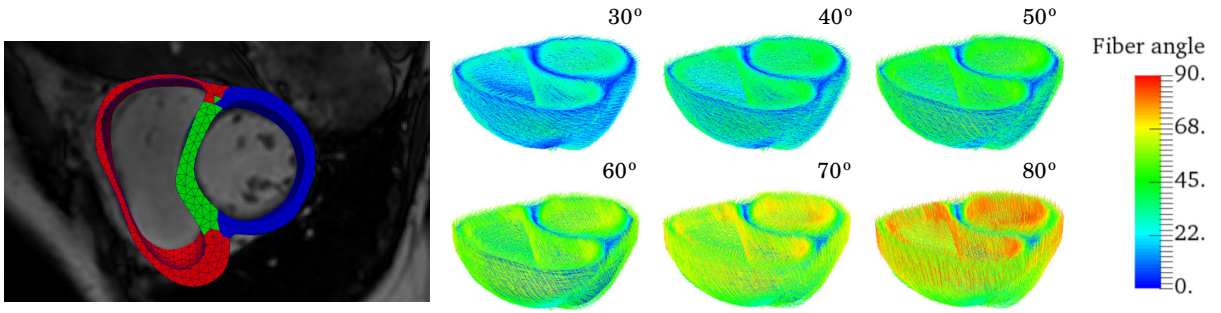

FIGURE 1 Left: finite element mesh of a biventricular geometry reconstructed from MR images separated into 3 material regions, namely, LVFW (blue), septum (green) and RVFW (right). Right: myocardial fiber orientation are assigned using the LDRB algorithm (Bayer et al. 2012) with an angle $+\alpha$ and $-\alpha$ prescribed on the endocardium and epicardium, respectively. Here showing the fiber architecture for α ranging from 30° to 80° with increments of 10°, where the absolute value of the fiber angle is used as color-map.

2.2 | Mechanical modeling

We consider a configuration of a biventricular continuum body $\mathfrak{B}$, which is a function $\kappa : \mathfrak{B} \to \mathbb{R}^3$, and denote the reference and current configurations by $\Omega_0 = \kappa_0(\mathfrak{B})$ and $\Omega = \kappa(\mathfrak{B})$, respectively. Letting $\mathbf{X}$ and $\mathbf{x}$ be the coordinates of a given material point in the reference and current configuration respectively, we have the corresponding displacement field $\mathbf{U} = \mathbf{x} - \mathbf{X}$, and the deformation gradient

$$\mathbf{F} = \frac{\partial \mathbf{U}}{\partial \mathbf{X}} + \mathbf{I}. \tag{1}$$

[1]https://bitbucket.org/mgenet/dolfin_dic

Mechanics of the heart wall was described using an active strain formulation (Ambrosi et al. 2011) that assumes a multiplicative decomposition of the deformation gradient,

$$\mathbf{F} = \mathbf{F}_e \mathbf{F}_a. \tag{2}$$

Here, $\mathbf{F}_a$ is associated with an inelastic deformation resulting from the actively contracting muscle fibers, whereas $\mathbf{F}_e = \mathbf{F}\mathbf{F}_a^{-1}$ is associated with the elastic deformation that preserves compatibility in the tissue, and passively carrying the mechanical load. We choose $\mathbf{F}_a$ to have the specific form

$$\mathbf{F}_a = (1-\gamma)\mathbf{f}_0 \otimes \mathbf{f}_0 + \frac{1}{\sqrt{1-\gamma}}(\mathbf{I} - \mathbf{f}_0 \otimes \mathbf{f}_0), \tag{3}$$

in which the parameter γ is associated with the relative active shortening along the muscle fibers. The same form of the active deformation gradient has previously been applied in e.g (Gjerald et al. 2014; Balaban et al. 2016).

We consider the transversely Holzapfel and Ogden hyperelastic material (Holzapfel and Ogden 2009) model that has the strain energy density function

$$\Psi(\mathbf{F}) = \frac{a}{2b}\left(e^{b(I_1-3)} - 1\right) + \frac{a_f}{2b_f}\left(e^{b_f(I_{4\mathbf{f}_0}-1)_+^2} - 1\right), \tag{4}$$

where the invariants are given by

$$I_1 = \operatorname{tr}\mathbf{C}, \quad I_{4\mathbf{f}_0} = \mathbf{f}_0 \cdot (\mathbf{C}\mathbf{f}_0). \tag{5}$$

Here $\mathbf{C} = \mathbf{F}^T\mathbf{F}$ is the right Cauchy Green tensor, and $\mathbf{f}_0$ denotes the unit fiber vector field in the reference configuration. Within the active strain formulation, the strain energy depends only on elastic deformations, and so the modified strain energy function $\Psi = \tilde{\Psi}(\mathbf{F}_e)$ was used instead.

For comparison, we also test the more frequently used active stress formulation (Hunter et al. 1998). In this formulation, the total Cauchy stress tensor is additively decomposed into a passive and an active component i.e.,

$$\boldsymbol{\sigma} = \boldsymbol{\sigma}_p + \boldsymbol{\sigma}_a, \tag{6}$$

where the passive stress tensor is given by

$$\boldsymbol{\sigma}_p = \frac{1}{J}\frac{\partial \Psi}{\partial \mathbf{F}}\mathbf{F}^T, \tag{7}$$

and the active stress tensor is given by

$$\boldsymbol{\sigma}_a = T_a\left[\mathbf{f} \otimes \mathbf{f} + \eta\left(\mathbf{I} - \mathbf{f} \otimes \mathbf{f}\right)\right]. \tag{8}$$

Here T_a is the magnitude of the active stress and η controls the amount of transverse active stresses. Although active stresses, in principle, develop along the fiber direction, studies have shown (Lin and Yin 1998) that active stresses in the transverse direction are non-negligible due to imperfect alignment of the muscle fibers. We therefore set $\eta = 0.2$ (Sundnes et al. 2014), and note that transverse active stresses are naturally embedded in the active strain formulation by requiring $\det \mathbf{F}_a = 1$.

Myocardium was assumed to be incompressible. The incompressibility was enforced in the model using a two-field variational approach, in which the term $-p(J-1)$ was added to the total strain energy with p denoting a Lagrange multiplier that represents the hydrostatic pressure. The deviatoric and volumetric mechanical responses were also uncoupled by multiplicatively decomposing the deformation gradient (Weiss et al. 1996),

$$\mathbf{F} = \mathbf{F}_{\text{iso}}\mathbf{F}_{\text{vol}} \tag{9}$$

and letting the strain-energy be a function of only isochoric deformations i.e., $\Psi = \bar{\Psi}(\mathbf{F}_{\text{iso}})$.

Ventricular base was fixed in the longitudinal direction and the biventricular geometry was anchored by constraining the epicardial surface using a Robin-type boundary condition with a linear spring of stiffness $k = 0.5$ kPa/cm^2 (Xi et al. 2016). Measured cavity pressure in the LV (p_{lv}) and RV (p_{rv}) were applied as a Neumann condition at the endocardial surfaces. The Euler-Lagrange equations in the Lagrangian form reads: Find $(\mathbf{U}, p) \in V \times Q$ such that for all $(\delta\mathbf{U}, \delta p) \in V \times Q$ and $(\mathbf{U} \cdot \mathbf{N})|_{\partial\Omega_0^{\text{base}}} = 0$,

$$\delta\Pi(\mathbf{U}, p) = \int_{\Omega_0} \left[\mathbf{P} : \nabla\delta\mathbf{U} - \delta p(J-1) - pJ\mathbf{F}^{-T} : \nabla\delta\mathbf{U} \right] \mathrm{d}V + \delta\Pi_{\text{ext}} = 0, \tag{10}$$

with

$$\begin{aligned}\delta\Pi_{\text{ext}} = &\int_{\partial\Omega_0^{\text{endo LV}}} p_{\text{lv}} J\mathbf{F}^{-T}\mathbf{N}\cdot\delta\mathbf{U}\mathrm{d}S \\ &+ \int_{\partial\Omega_0^{\text{endo RV}}} p_{\text{rv}} J\mathbf{F}^{-T}\mathbf{N}\cdot\delta\mathbf{U}\mathrm{d}S + \int_{\partial\Omega_0^{\text{epi}}} k\mathbf{U}\cdot\delta\mathbf{U}\mathrm{d}S.\end{aligned} \tag{11}$$

Here $V = H^1(\Omega_0)$, completed with homogeneous Dirichlet boundary data, $Q = L^2(\Omega_0)$, $\mathbf{N}$ is the outward pointing unit normal and $\mathbf{P}$ is the first Piola-Kirchhoff stress tensor.

For an incompressible, hyperelastic, continuum body, the total Cauchy stress tensor is given by

$$\boldsymbol{\sigma} = \frac{1}{J}\frac{\partial\Psi(\mathbf{F})}{\partial\mathbf{F}}\mathbf{F}^T - p\mathbf{I}. \tag{12}$$

With the decoupling of the isochoric and volumetric deformation according to (9), the first term in (12) represents the deviatoric stresses and p is the hydrostatic pressure. Myofiber stress was computed by first a push forward of the fiber field to the current configuration, $\mathbf{f} = \mathbf{F}\mathbf{f}_0$, and then an inner product with the stress tensor $\boldsymbol{\sigma}_{\mathbf{f}} = \mathbf{f}\cdot\boldsymbol{\sigma}\mathbf{f}$. The average fiber stress in a given region Ω_j was computed by integrating the fiber stress over that region and dividing by the volume i.e., $\overline{\boldsymbol{\sigma}_{\mathbf{f}}}^{\Omega_j} = |\Omega_j|^{-1}\int_{\Omega_j}\boldsymbol{\sigma}_{\mathbf{f}}\mathrm{d}V$.

2.3 | PDE-constrained optimization

The ventricular mechanics model outlined in Section 2.2 contains model parameters that may vary from individual to individual. Calibration of these model (or control) parameters was achieved by solving a PDE-constrained optimization problem, where we minimized a cost functional representing the mismatch between the simulated and observed data, subject to the constraint of satisfying (10)-(11). The minimization problem can be formally stated as

$$\begin{aligned}\underset{m}{\text{minimize}} \quad & \mathcal{J}((\mathbf{U}, p), m) \\ \text{subject to} \quad & \delta\Pi(\mathbf{U}, p) = 0.\end{aligned} \tag{13}$$

Here $\mathcal{J}$ is the objective functional that we want to minimize, which depends on the state variable $(\mathbf{U}, p)$ and the control parameter(s) m. The state variables may also depend on the control parameters $(\mathbf{U}, p) = (\mathbf{U}(m), p(m))$. To ease notation, this dependency is not explicitly stated here.

Minimization of the cost functional $\mathcal{J}$, should bring the simulated results closer to the clinical observations. Therefore, $\mathcal{J}$ should reflect a distance between the simulated results and the observed data. Given a measurement point i, let $(\mathbf{U}^i, p^i)$ be the simulated state variables at that point, and let m^i represents any generic model parameter, that we want to estimate. The cost functional is then given by

$$\mathcal{J}((\mathbf{U}^i, p^i), m^i) = \alpha\mathcal{J}_{\text{volume}}((\mathbf{U}^i, p^i), m^i) + \beta\mathcal{J}_{\text{strain}}((\mathbf{U}^i, p^i), m^i) + \lambda\mathcal{J}_{\text{reg}}(m^i). \tag{14}$$

The first two terms represent the mismatch between simulated and observed strains and volumes, whereas $\mathcal{J}_{\text{reg}}$ is a regularization term that penalizes non-smooth values of the control parameter m^i for numerical stability. The weights α, β and λ control what terms is favored in the optimization.

The cavity volume was given by

$$\tilde{V}_{\cdot} = -\frac{1}{3}\int_{\partial\Omega_0^{\text{endo}\ \cdot}} (\mathbf{X}+\mathbf{U})J\mathbf{F}^{-T}\mathbf{N}\mathrm{d}S. \tag{15}$$

This equation holds as long as the base remains flat and is located at the $x = 0$ plane. We let $\mathcal{J}_{\text{volume}}$ be the sum of the squared relative volume error in each chamber:

$$\mathcal{J}_{\text{volume}}((\mathbf{U}^i, p^i), m^i) = \left(\frac{V_{\text{LV}}^i - \tilde{V}_{\text{LV}}^i}{V_{\text{LV}}^i}\right)^2 + \left(\frac{V_{\text{RV}}^i - \tilde{V}_{\text{RV}}^i}{V_{\text{RV}}^i}\right)^2. \tag{16}$$

Here, $(\tilde{V}_{\text{LV}}, \tilde{V}_{\text{RV}})$ and $(V_{\text{LV}}, V_{\text{RV}})$ are the simulated and measured cavity volumes, respectively.

Volumetric averaged strains were computed in each material region (i.e., LVFW, RVFW and septum) using end-diastole (ED) as reference. Letting $\mathbf{F}_{\mathrm{ED}}$ be the deformation gradient tensor associated with ED, the Green-Lagrange strain tensor with ED as reference was given by $\tilde{\mathbf{E}} = \frac{1}{2}(\mathbf{F}^T\mathbf{F}_{\mathrm{ED}}^{-T}\mathbf{F}\mathbf{F}_{\mathrm{ED}}^{-1} - \mathbf{I})$. Averaged normal strain along the circumferential direction $\mathbf{e}_{\mathrm{circ}}$ in material region Ω_j was defined by

$$\tilde{\varepsilon}_j = \frac{1}{|\Omega_j|}\int_{\Omega_j} \mathbf{e}_{\mathrm{circ}} \cdot \tilde{\mathbf{E}}\mathbf{e}_{\mathrm{circ}} \mathrm{d}V. \tag{17}$$

Correspondingly, the strain mismatch functional was given by the total squared error between the simulated circumferential strain $\tilde{\varepsilon}_j^i$ and the measured circumferential strain ε_j^i over all material regions

$$\mathcal{J}_{\mathrm{strain}}((\mathbf{U}^i, p^i), m^i) = \sum_{j=1}^{N} \left(\varepsilon_j^i - \tilde{\varepsilon}_j^i\right)^2. \tag{18}$$

Finally, the regularization term was defined as the total squared distance from the mean value, that is if $m^i = (m_1, \cdots, m_N)$, then

$$\mathcal{J}_{\mathrm{reg}}(m^i) = \sum_{j=1}^{N}(m_j^i - \overline{m}^i)^2, \qquad \overline{m}^i = \frac{1}{N}\sum_{j=1}^{N} m_j^i. \tag{19}$$

As noted above, the purpose of this term is to avoid numerical instabilities by penalizing large variations in the control parameters.

The functional gradient

$$\frac{\mathrm{d}\mathcal{J}}{\mathrm{d}m} = \frac{\partial \mathcal{J}}{\partial m} + \frac{\mathrm{d}\mathcal{J}}{\mathrm{d}\mathbf{w}}\frac{\partial \mathbf{w}}{\partial m}, \qquad \mathbf{w} = (\mathbf{U}, p) \tag{20}$$

points in the direction of steepest descent and is required in gradient-based optimization methods. While the terms $\frac{\partial \mathcal{J}}{\partial m}$ and $\frac{\mathrm{d}\mathcal{J}}{\mathrm{d}\mathbf{w}}$ are typically straightforward to compute, the term $\frac{\partial \mathbf{w}}{\partial m}$ cannot be computed easily, since the state variable $\mathbf{w}$ can only be determined by solving the forces-balance equation (10). Specifically, estimating this term with N control parameters using a finite difference approach will require one to solve the (typically computational expensive) force-balance equation N+1 times, becoming impractical when N is large. Instead, it is possible to transform the system of equations into its adjoint system, where the gradient is given by

$$\frac{\mathrm{d}\mathcal{J}}{\mathrm{d}m} = \frac{\partial \mathcal{J}}{\partial m} - z^* \frac{\partial(\delta\Pi)}{\partial m}, \tag{21}$$

with $(\cdot)^*$ referring to the adjoint (or Hermitian transpose) and z is the solution of

$$\left(\frac{\partial(\delta\Pi)}{\partial \mathbf{w}}\right)^* z = \left(\frac{\partial \mathcal{J}}{\partial \mathbf{w}}\right)^*. \tag{22}$$

We can therefore solve the adjoint equation first (22), and then compute the functional gradient by plugging the solution z into (21). Hence, computing the functional gradient using the adjoint approach requires only one additional solve of a linearized system that is independent of the number of control parameters.

2.4 | Parameter estimation

The pipeline for fitting the model to patient data was divided into two sequential phases; a passive phase where we estimated the material parameters that define the passive behavior of the myocardium, and an active phase where we estimated the amount of active contraction. In both cases, the control parameters were spatially resolved. During the passive phase the control parameter was allowed to vary spatially on the LV (LVFW+septum) and RV segments, while in the active phase the LV was separated into LV free wall and septal segments, which provided additional degrees of freedom to allow for non-homogeneous LV contraction.

Geometries used in the simulation were reconstructed from medical images. These geometries are, in principle, not load-free. Hence, we need to estimate the unloaded (zero pressure) geometries, which will revert back to the original reconstructed geometries when loaded with the measured pressure. Several methods exists for estimating the unloaded geometry (Govindjee and Mihalic 1996; Gee et al. 2010). Among the most simplest ones is the backward displacement method (Sellier 2011; Bols et al. 2013) that can also be used to incorporate residual stresses into the finite element models by simulating tissue growth (Genet et al. 2015b). Nevertheless, this inverse problem (of finding the unloaded geometry) has been shown to produce non-unique solutions, especially when buckling is present (Govindjee and Mihalic 1996), although relaxation techniques can be used to improve convergence and stability (Rausch et al. 2017). For the case of a bi-ventricular geometry, buckling may occur due to the thin RVFW and a high RV pressure. For this reason, we choose a simpler approach to estimate the unloaded configuration. As shown in the left of Figure 2 , we start by applying one iteration of the backward displacement method with initial values prescribed for the material parameters followed by the

material parameter estimation as outlined below. This will result in a deflated geometry as shown in the right of Figure 2 . A sensitivity analysis (APPENDIX A:) was conducted to assess how the choice of the initial material parameter values affects our results.

Four material parameters i.e., a, a_f, b and b_f (4) have to be estimated in the passive phase. Due to the sparsity of passive data used for the optimization, if we let all these parameters vary freely, we may end up in a situation where multiple parameter sets will equally minimize the cost functional, and the optimal control will depend heavily on the initial guess of the optimization. We therefore restricted our control parameter to be only the linear isotropic parameter with an initial guess $a = 1.291$kPa, and have the remaining parameters fixed according to (Asner et al. 2015, Table 2, case P2). The weights were set $\alpha = 1.0, \beta = 0.0$ and $\lambda = 10^{-6}$ in (14) so that only ED volumes were used for fitting. Since fitting the left and right ventricular end diastolic volumes might require different material properties of the left and right ventricular wall, the parameter a was spatially resolved with one parameter associated with the LV (LVFW + septum) and one parameter associated with the RVFW

In the active phase, the optimized passive material parameters were fixed and the relative active fiber shortening γ in (3) was chosen as control parameter. For this phase, the weights in (14) were set to $\alpha = 0.1, \beta = 1.0$ and $\lambda = 10^{-4}$, so that both strain and volume are considered in the optimization. This choice of weighting was made ad hoc, reflecting the relative size of the different terms in the cost functional. It should also be noted that the volume functional in (16) is a relative error while the strain functional in (18) represents a total error. The cost function parameter values were taken from Balaban et al. (2016), where they were chosen based on an L-curve type analysis.

For each time point, we estimated γ locally in the LVFW, RVFW and septum. The initial guesses for the optimization were set to zero in the first iteration. In subsequent iterations, the initial guesses were set to the optimized values found in the previous iteration. Note that in the case when active stress formulation was used instead, the parameter T_a in (8) was used as the control parameter and estimated in a similar fashion. A schematic illustration of the full optimization pipeline is provided to the left in Figure 2 .

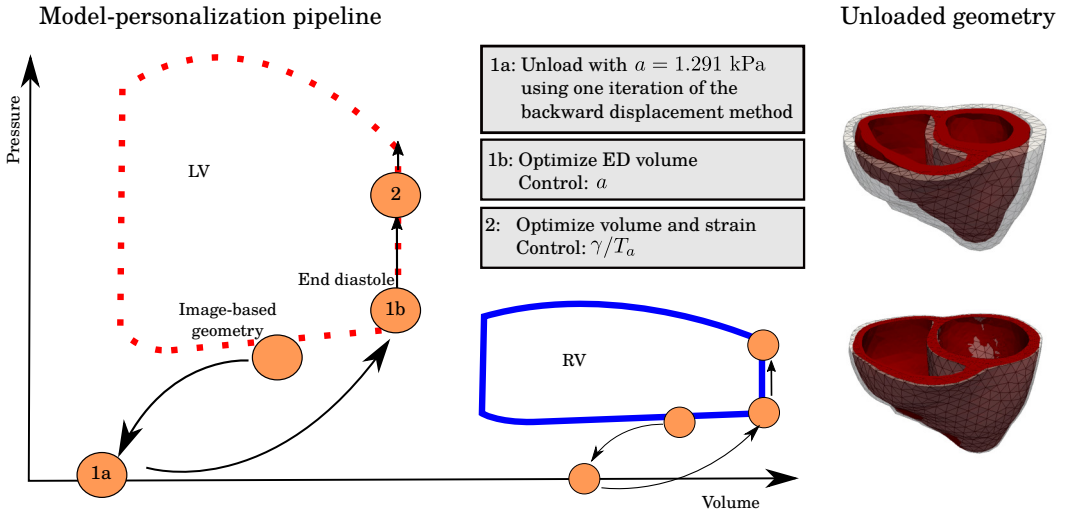

FIGURE 2 To the left we see the model-personalization pipeline. The image-based geometry corresponds to some image frame taken at mid diastole. An estimate of the unloaded geometry was found by applying one iteration of the backward displacement method using $a = 1.291$ kPa according to (Asner et al. 2015), followed by an estimation of a by minimizing the fit of the end-diastolic volumes. During systole, both cavity volumes and circumferential strain were used in the optimization to determine the amount of active contraction in terms of the active control, which are respectively γ and T_a in the active strain and active stress formulation. To the right we show a comparison of the unloaded geometry for CASE3. The upper figure shows the resulting unloaded, zero pressure geometry in red and the the original image-based geometry in transparent, while the bottom figure shows the unloaded geometry, inflated to the target pressure in the image-based geometry, and the original image-based geometry in transparent for comparison.

The control parameter in the active phase represents an index of contractility (Finsberg et al. 2017), meaning that the higher the value of the control parameter, the more forcefully the myocardium is trying to contract against the external loads. To separate between the LV and RV contractility, we extracted the average value of this control parameter in these two segments. Another index of contractility is the end systolic elastance (Sagawa et al. 1977), which we have also estimated in the LV and RV by perturbing the loading conditions at the end systolic state and estimate the slope of the resulting pressure-volume relationship (Finsberg et al. 2017).

TABLE 1 Timings for evaluation (eval) of the forward model and the gradient, running on one computing node with 8 cores for the different subjects with different mesh resolutions. The average number of forward and gradient evaluations for each measurement points are also shown along with the standard deviations.

Patient ID	# elements	forward eval time (s)	# forward eval	gradient eval time (s)	# gradient eval	Total run time (h)
CASE1	7362	32 ± 19.8	9 ± 1.6	9 ± 0.1	8 ± 1.5	1.97
	58896	668 ± 529.8	9 ± 1.7	81 ± 1.3	7 ± 1.6	36.1
CASE2	4755	19 ± 9.6	9 ± 2.1	8 ± 0.1	8 ± 2.0	1.88
	38040	387 ± 325.8	9 ± 2.5	47 ± 0.4	8 ± 2.2	32.6
CASE3	4377	17 ± 5.3	10 ± 2.1	8 ± 0.9	8 ± 2.1	1.35
	35016	259 ± 146.3	9 ± 2.4	42 ± 0.7	8 ± 2.2	15.6

2.5 | Implementation details

The force-balance equations of this incompressible nonlinear elasticity problem were solved using the finite element method with Lagrange elements. More specifically, the displacement and hydrostatic pressure fields were interpolated using piecewise quadratic and linear Lagrange basis functions, respectively. These mixed elements, known as the Taylor-Hood finite elements (Hood and Taylor 1974), are known to satisfy the discrete inf-sup condition (Chapelle and Bathe 1993) and leads to a stable discretization. The solver was implemented in FEniCS (Logg et al. 2012), which is an open-source platform for solving PDEs using the finite element method. Nonlinear systems of equations were solved using Newton's method, and a distributed memory parallel LU solver(Li and Demmel 2003) was used to solve the linear systems.

To solve the optimization problem (13) we applied a sequential quadratic programming algorithm (SQP) (Kraft et al. 1988). This gradient-based optimization algorithm requires the functional gradient (20). This gradient was computed by solving an automatically derived adjoint equation using dolfin-adjoint (Farrell et al. 2013). The full source code is publicly available[2].

3 | RESULTS

In this section we present the results from the model personalization process. Results of the data matching are presented in Section 3.1, together with a validation of the model and analysis of the solver performance. To validate the model we compare the simulated and measured longitudinal strain which was not used in the optimization. In Section 3.2 we present the results of the extracted mechanical features such as indices of contractility and fiber stress. We also investigated the efficiency of the algorithm and the effect of mesh refinement, and found that the chosen refinement level was sufficient to yield convergent solutions.

3.1 | Data assimilation, validation and solver performance

The simulated and measured pressure-volume (PV) loops of the RV and LV, as well as circumferential strain in the LV, septum and RV are shown in Figure 3 . We found that the fit of the data was highly dependent on the choice of fiber angles, which affects both volume change and circumferential shortening. Plotting the average value of the volume cost functional (as defined in (16)) for each choice of fiber angles (see the upper right panel in Figure 3) revealed that the optimal value of α lies in the range $70^\circ - 80^\circ$ for all 3 cases.

Although available, we chose not to use longitudinal strain data in the optimization. Therefore, the comparison of model-predicted longitudinal strain with the measurements serves as a validation of the model-personalization process. The simulated and measured LV longitudinal strain curves are shown in Figure 4 . We note that the fit in all regions was again highly sensitive to the choice of fiber angle. Choosing $\alpha = 70^\circ$ produced the best fit for the LV longitudinal strain for CASE1 and CASE3, while an angle 60° gave the best fit for CASE2. The Septal and RV longitudinal strain was best fitted with $\alpha = 80^\circ$.

We further evaluated the solver performance in the optimization process. In this work, all computations were performed on a computing cluster using one node with 8 cores. In Table 1 we present timings for evaluation of the forward model (i.e., evaluation of the cost functional), timings for evaluation of the gradient, as well as the average number of such evaluations and the standard deviations. These timings are shown for optimizations using the original and refined meshes with a fiber angle of 60°.

[2]https://bitbucket.org/finsberg/pulse_adjoint

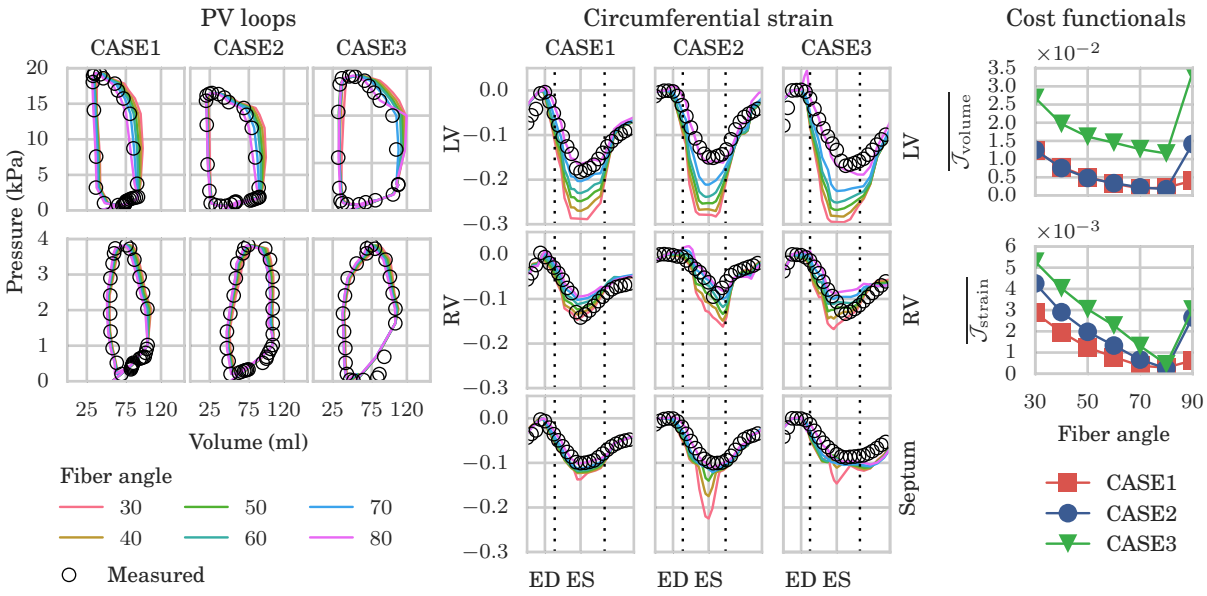

FIGURE 3 Results of the gradient-based minimization of model-data mismatch for different choice of fiber angles. Left: simulated (color lines) and measured (black circles) PV loops in the LV (top row) and RV (bottom row). Center: simulated (color lines) and measured (black circles) circumferential strain in the LV (top row), RV (middle row) and septum (bottom row). Right: average values of cost functional for the volume (top row) and strain (bottom row), for each choice of fiber angle.

3.2 | Mechanical analysis

3.2.1 | Cardiac contraction

The estimated active strain parameter γ in (3), which served as the control parameter during the optimization in the active phase, is plotted for various fiber angles to the left in Figure 5 . This parameter varies regionally in the LVFW, septum and RVFW, but is shown here as an average in the LV containing LVFW + septum (top) and RV containing only RVFW (bottom). As shown in the figure, time-variation and magnitude of γ were similar in the 3 cases and insensitive to the prescribed fiber angles.

Time traces of the active strain parameter γ found in the LV and RV are plotted together for the 60° fiber angle case in the left of Figure 6 in order better compare their differences. A similar plot of the active stress parameter T_a in logarithmic scale is also shown in the same figure. As shown in the figure, the time-variations of T_a and γ, which are indices of cardiac contractility, were largely similar between the LV and RV with peak values located approximately at end-systole. Peak values found in the RV were, however, lower than those found in the LV. These findings were consistent across all the 3 cases. A similar plot in Figure 7 shows that the active strain γ is insensitive to the mesh resolutions listed in Table 1

3.2.2 | Fiber stress

Time traces of the average Cauchy fiber stress are shown on the right of Figure 5 for different fiber angle variations. Only very small variations in the average fiber stress were found with respect to the choice of fiber angle in the optimization process. Snap shots of the fiber stress distribution at ED and ES are plotted in Figure 8 for the 60° fiber angle case. Regional variation of fiber stress was largely consistent between the 3 cases with pockets of high and low stresses found, respectively, at the apex-epicardial and endocardial regions at ES.

In Figure 6 , we compare the average fiber stress time variation found using the two different active contraction formulations, either active strain or active stress. As shown in the figure, fiber stress in the RV computed using active stress and active strain formulations behaved similarly with time. Similar regional variation was also found where both formulations predicted higher fiber stress in the LV than the RV. Peak fiber stress predicted in the LV, however, was different in the two formulations with higher stress occurring at isovolumic relaxation in the active stress formulation.

The specific average value of the end-diastolic and end systolic fiber stress for the case of a 60° fiber angle are displayed in Table 2 , showing small variability between patients, despite differences in individual PV loops.

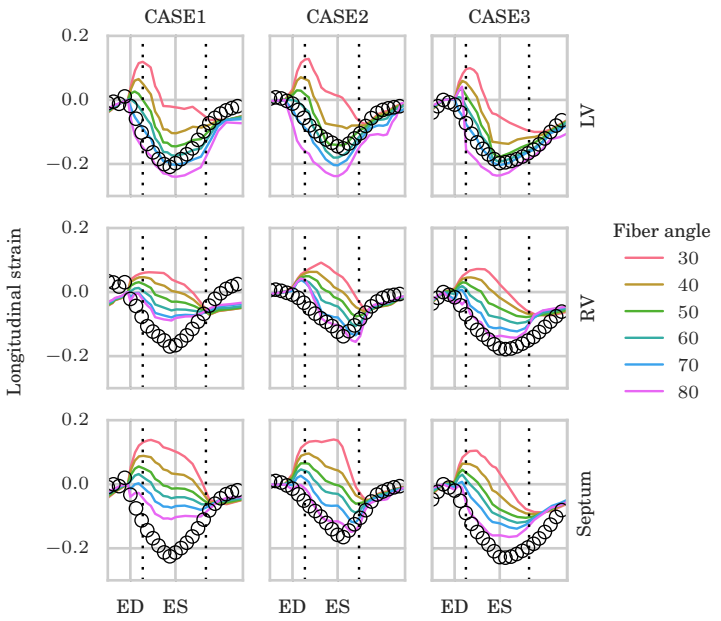

FIGURE 4 Validation of the model-personalization process using simulated and measured longitudinal strain which was not used in the optimization. Upper, middle and lower panel show the longitudinal strain curves for different choice of fiber angles in the LV, RV and septum respectively.

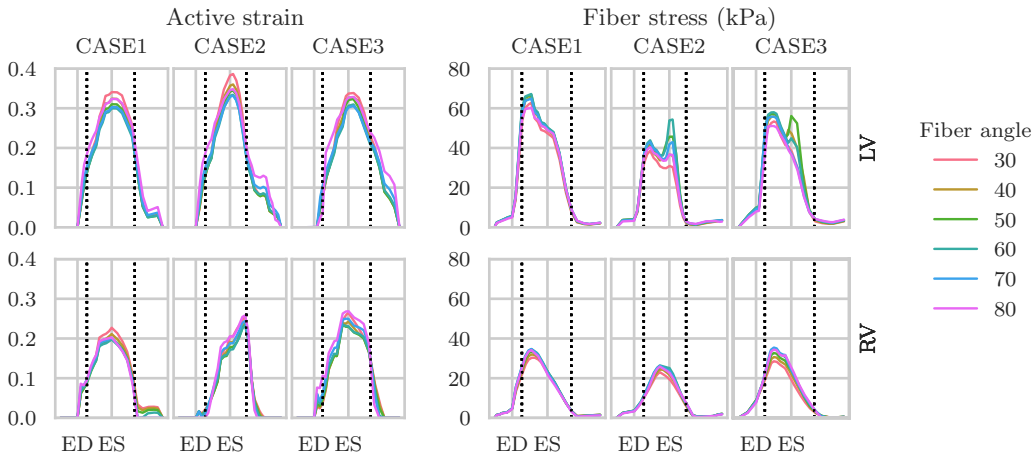

FIGURE 5 To the left, average traces of the active strain parameter γ in (3) in the LV (top) and RV (bottom) for different choice of fiber angle. To the right average traces of Cauchy fiber stress in the LV (top) and RV (bottom) for different choice of fiber angle. The fiber angles were defined symmetrically across the wall with a negative angle on the epicardium and a positive angle on the endocardium ranging from $30° - 80°$ with increments of $10°$. On the $x-$axis we plot the normalized time with respect to end-diastole (ED) and end-systole (ES). Horizontal dotted lines indicate timings of opening of the aortic and mitral valve.

TABLE 2 Average LV and RV fiber stress and end diastole and end systole

Patient ID	LV (ED)	RV (ED)	LV (ES)	RV (ES)
CASE1	5.76	4.87	48.3	19.2
CASE2	4.04	3.57	54.4	22.7
CASE3	9.94	8.34	40.3	18.2
Average $\pm$ std	6.58 ± 2.48	5.59 ± 2.01	47.65 ± 5.74	20.03 ± 1.91

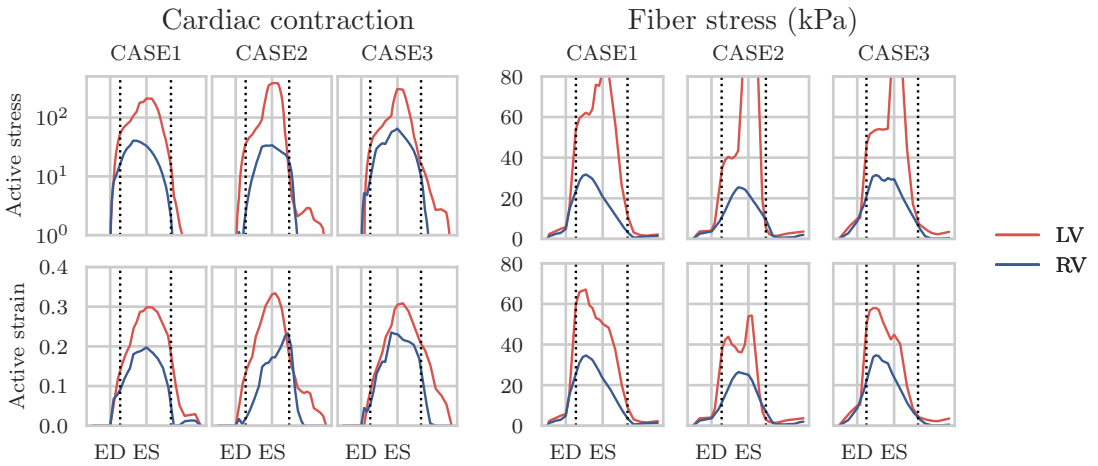

FIGURE 6 Comparison of fiber stress and cardiac contraction using the active strain and active stress approach using $60°$ fiber angle. To the left, average traces of the active stress (top) parameter T_a in (8), and the active strain (bottom) parameter in 3. The active stress parameter, with unit kPa, is plotted on a logarithmic scale for easier comparison with the active strain parameter. To the right, estimated Cauchy fiber stress using the active stress (top) and active strain formulation (bottom). On the $x-$axis we plot the normalized time with respect to end-diastole (ED) and end-systole (ES). Horizontal dotted lines indicate timings of opening and closing of the aortic valve.

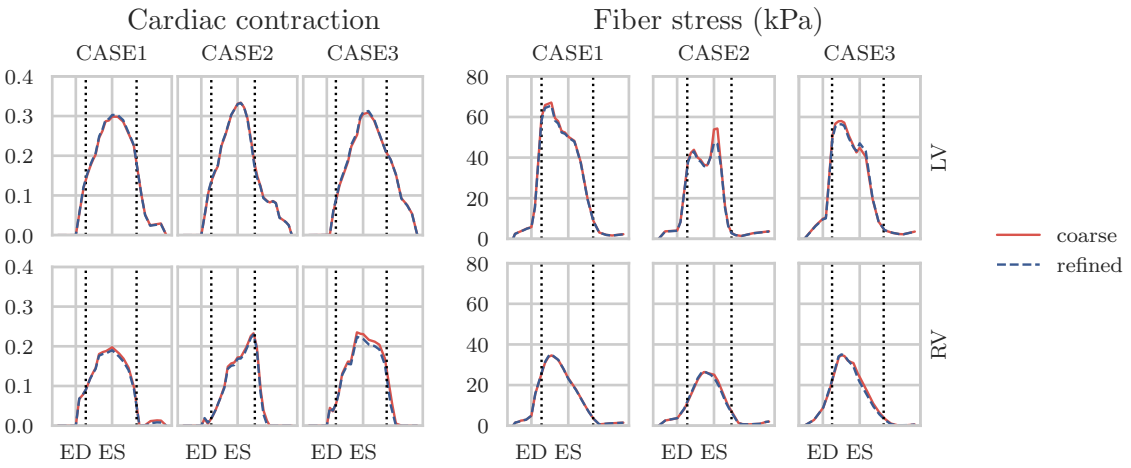

FIGURE 7 Results obtained using different mesh resolutions as listed in Table 1 . To the left and right respectively, the active strain and fiber stress traces, in the LV (top) and RV (bottom) estimated using the coarse and refined geometry.

3.2.3 | Ventricular Elastance

Table 3 shows the estimates of ES elastance in the LV and RV that were computed using the active strain formulation. The table shows the average $\pm$ one standard deviation of the ES elastance over various fiber angles. Elastance was consistently found to be ~ 10 times larger in the LV than in the RV, and was largely insensitive to the prescribed fiber angle as indicated by the small standard deviation.

4 | DISCUSSION

In this study, we have presented a novel and highly efficient method for non invasive personalization of an image-based bi-ventricular mechanics model based on regional measurements of circumferential strain, as well as global measurements of volumes and pressures in the LV and RV. A

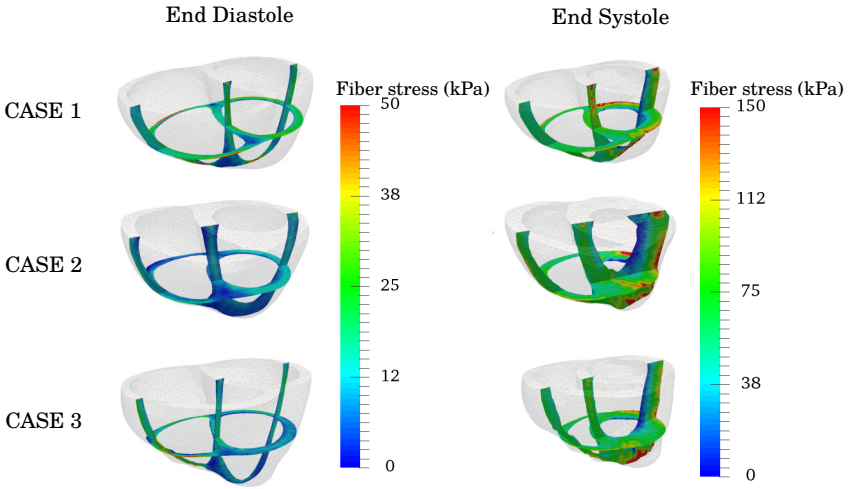

FIGURE 8 Snap shots of the end diastolic and end systolic configuration and the estimated fiber stresses shown as color-map.

TABLE 3 LV and RV end-systolic elastances estimated by perturbation of model at the end-systolic state. Average values and standard deviation with respect to varying fiber angle are shown.

Patient ID	LV (kPa/ml)	RV (kPa/ml)
CASE1	1.96 ± 0.06	0.23 ± 0.02
CASE2	1.94 ± 0.14	0.18 ± 0.01
CASE3	1.52 ± 0.07	0.21 ± 0.01

gradient based optimization method was used to minimize the model-data mismatch by solving a PDE-constrained optimization problem for each measurement point in order to calibrate model parameters. Passive material parameters and an unloaded (zero-pressure) geometry were estimated using the bi-ventricular geometry that was reconstructed from MR images acquired at late diastole. Time variation of an active contraction parameter was estimated throughout the cardiac cycle starting from ED.

This framework was applied using measurements from three normal subjects to extract estimates of regional fiber stress as well as indices of myocardial contractility. Sensitivity analysis of the model outputs with respect to the choice of fiber angle distribution, mesh resolution and active formulation were also conducted. The described framework is effective and efficient in capturing cardiac mechanical behavior throughout the cardiac cycle, and gave low patient-to-patient variabililty in the extracted mechanical features. As such, it has potential clinical utility in the quantification of contractile function and myocardial stress *in vivo* and the potential differentiation of pathological states.

4.1 | Data compatibility and multi-objective optimization

The objective functional in problem (13) consists of a weighted sum of different objective functionals. Such problems are referred to as multi-objective optimization problems (Marler and Arora 2004). While it is possible to perfectly match the strain or volume data individually with the chosen control parameters (data not shown), there is expected to be a trade-off when fitting both the volume and strain data in a combined objective functional. In such cases, a single, unique optimum does not always exist, but rather a family of so called Pareto optimal solutions can be found (Marler and Arora 2004). The particular solution found will depend on the chosen weights of each objective.

In a previous study (Balaban et al. 2016), the weights in the total functional given in (14) were determined by performing an exhaustive search, testing several combinations of weights of the strain and volume functionals, and choosing the corner-point of strain versus volume error curve. However, the weights will depend on the data source, and in our case choosing the weights proposed in (Balaban et al. 2016), resulted in an excellent fit of the volume, while a relatively poor fit of the strain, and hence a higher weight was chosen for the strain. Nevertheless, neither was captured exactly, and which data source is more important for model utility remains to be determined. In addition, other general methods for solving multi-objective optimization problems (Marler and Arora 2004) may be superior to the weighted sum method used here, and will be considered in future studies.

4.2 | Effect of mesh resolution

As shown in Table 1 , the total run time is substantially larger for a refined mesh (35 000 - 60 000 elements) compared to a coarser mesh (4000 - 8000 elements). Since computing time is an important factor that may limit the application of computational models in the clinic, we have investigated the accuracy of our predictions from the coarse meshes. Our results show that the accuracy of the extracted features related to cardiac contraction and fiber stress are not very sensitive to mesh resolution beyond the coarsest levels of $\sim$ 4000 elements. As seen in Figure 7 , the fiber stress and active strain traces obtained on the coarse and fine meshes are very similar, indicating that the coarsest meshes give sufficient accuracy for the extracted mechanical features.

4.3 | Fiber angle sensitivity

In this work, we applied a rule-based algorithm (Bayer et al. 2012) to assign myocardial fiber orientations to the bi-ventricular geometries, and investigated the sensitivity of the data matching and the extracted mechanical features to the choice of fiber field. Different fiber fields, in which the fiber angle varies linearly across the myocardium wall from α at the endocardium to $-\alpha$ at the epicardium were tested, for the range $30^\circ \leq \alpha \leq 80^\circ$. Our results show that α has to be in the upper part of the range i.e., $70 - 80^\circ$, in order to fit the PV loop and circumferential strain measurements simultaneously. The validation study (Section 3.1), where we compared our model results with the longitudinal strain, confirms this finding.

This highlights a major challenge in building accurate mechanics models of the myocardium. The choice of fiber field is very important, as it controls the amount of longitudinal and radial shortening during contraction. Unless the correct fiber field is used, strain measurements cannot be reproduced simultaneously in the model with the measured pressure volume relationships. Accurate measurements of the underlying ventricular microstructure are lacking, however, and therefore, rule-based methods (Bayer et al. 2012) are often the only alternative to prescribe muscle fiber field in subject-specific modeling of cardiac mechanics. Our fundamental knowledge of the myocardial architecture is based largely on early histological studies (Streeter et al. 1969), which found that the muscle fiber orientation varies linearly across the myocardial wall with an angle $\alpha = 60^\circ$ at the endocardium $\alpha = -60^\circ$ at the epicardium. This fiber field is often prescribed in ventricular models without questioning. On the other hand, diffusion tensor MRI (DT-MRI) is now becoming an important tool to measure fiber orientations and could potentially do so *in vivo* (Toussaint et al. 2013).

More recent histological studies (LeGrice et al. 1995) on the canine left ventricle have shown that the muscle fibers are more longitudinally oriented at the subendocardium and subepicardium than those obtained using DT-MRI, and such fiber orientation can better reproduce the longitudinal motions observed in the experiments(Wang et al. 2015). Our results support this finding.

A few hypotheses on the basis of cardiac muscle fiber orientation in the ventricles have been put forward. For example, it has been hypothesized that myocardial fiber orientations adapts to achieve a minimal fiber-cross fiber shear strain during the cardiac cycle (Kroon et al. 2009). While our results showed that the active strain parameter γ varied a little with respect to the different fiber angle α prescribed in the model, they also show that the peak active strain γ is lowest when α lies between 60° and 70° in all 3 cases. This finding suggests that the tight range of α found here is optimal in the sense that the active shortening necessary to produce the same stroke volume is at its minimum.

4.4 | Fiber stress

As there is no direct way to measure myocardial fiber stresses, we have compared our results with other patient specific modeling studies. The range of reported values for humans are broad, and are mostly confined to the LV. For example, (Genet et al. 2014) reported fiber stress computed at ED (2.21 ± 0.58kPa) and ES (16.64 ± 4.73kPa) in normal humans, whereas (Scardulla et al. 2016) conducted a stress analysis on healthy bi-ventricles and found that wall stress at ES was 65.7 ± 12.3 kPa in the LV and 23.6 ± 14.2 in the RV.

Our estimated average fiber stresses (Table 2) are well within the range of values reported in these studies. Fiber stress distributions at ED and ES (Figure 8) are also consistent in the three subjects investigated here. Furthermore, our results also show small variations in fiber stress with respect to the choice of fiber field. Fiber stresses obtained from active strain and stress formulations are also comparable during late diastole and early systole. A large difference in the fiber stress between these two formulations, however, can be found at late systole and during the isovolumic relaxation when the ventricles are in their most compressed state. In particular, the active stress formulation produces elevated stresses during this time interval. The same phenomenon was observed in a sensitivity analysis (APPENDIX A:) on the initial passive material parameter a used to find the unloaded geometry. We found that the elevated stresses are always accompanied by very high hydrostatic pressure p, suggesting that the enforcement of incompressibility, which does not hold *in vivo* due to blood perfusion in the myocardial wall, is causing this artifact. Future studies are needed to examine the effect of compressibility to our results.

4.5 | Contractility

Higher value of the active strain parameter γ or the active stress parameter T_a indicates that the myocardium is contracting more forcefully and our results also suggest that the LV generates a higher contractile force per myocardial volume than the RV. One of the underlying mechanisms that modulate the contractile forces is calcium dynamics (Hunter et al. 1998; Ambrosi et al. 2011), and while T_a and γ cannot be directly compared to the calcium concentration because of the difference in units, their time traces have similar shapes when compared to the calcium transient. This finding is independent of the prescribed fiber field and the initially assigned passive material parameter a, as shown in APPENDIX A:. Further investigation of these estimates is needed, but we hypothesize that these measurements may provide useful biomarkers. Due to the observed consistent results in normal patients, even for wide ranging PV loops, these estimates of contractility could therefore potentially serve as important diagnostic estimates in cases where disease alters myocardial contractility.

4.6 | Elastance

End systolic elastance is widely recognized as an important determinant of systolic function (Sagawa et al. 1977). However, it's use in clinical practice is limited due to the need for invasive measurements of pressure and volume in response to varying loading conditions.

In the present work we have simulated a change in loading condition by perturbing only the ES pressure (keeping all other quantities fixed), and computing the ES elastance from the slope of the resulting pressure-volume relationship. This approach has previously been applied to obtain LV ES elastance (Finsberg et al. 2017), but has not been applied to find RV ES elastance in bi-ventricular geometries.

The resulting LV ES elastances range from approximately 1.0 to 2.0 kPa/ml. These values are higher than previous measurements in healthy human hearts, which range from 0.26 to 0.4 kPa/ml (Chen et al. 1998).

There are few reported values of normal human RV elastance. However, (Brown and Ditchey 1988) reported values of the maximal RV elastance in the range of 0.32 -1.23 mmHg/ml/m^2 in normal humans. Using a body surface area of 2 m^2 (typical in humans), this range translates to 0.08 - 0.32 kPa/ml. Our estimated values ~ 0.2 kPa/ml is well within this range. It should be noted here that our estimated values of ES elastance do not take into account any physiological responses of the tissue, such as a change in active tension in response to an increased load. As such, these values represent only a local estimate of the elastance, since all other quantities were held fixed during the perturbation of the pressure. Because of these limitations, our elastance estimate will make most sense in the active strain formulation as a force-length dependence is implicitly included in this formulation. No such relation is, however, included in the simple active stress model here. Correspondingly, the active stress does not change as the load is perturbed, which may lead to an underestimation of the elastance.

4.7 | Limitations and future directions

In this work, we clearly see a variability of model-data fit with respect to choice of the fiber angle, suggesting that the fiber field can be calibrated to better fit the data. Here, we have only prescribed a linear transmural fiber angle variation that has opposite signs at the endo- and epicardium in both LV and RV. Dissection studies, however, generally found that the fibers are more circumferentially oriented at the subepicardium and more longitudinally orientated at the subendocardium in the RV (Ho and Nihoyannopoulos 2006). This suggests that one should also consider non-symmetric fiber fields across the wall as well as different fiber field in the LV and RV. We seek to investigate these issues in future studies, possibly together with in vivo measures of fiber angles.

As noted above, the constants that balance the terms of the cost functional (14) were adjusted based on a previous study Balaban et al. (2016) of a single LV, where an L-curve type analysis was performed to estimate an optimal set of weights. Since the present study also considers the RV and the current cost functional form differs from the LV case, it is likely that these differences may affect the optimal choice of weight parameters. Hence, although the chosen parameter values gave good results for our applications here, there may exist even better choices.

While we were able to obtain stress measures across a small cohort of healthy subjects that were both internally consistent as well as in broad agreement with other published studies, the effect of our modelling assumptions remains to be determined. Here we used an incompressible model of the myocardium, even though it is well known that the myocardium is compressible due perfusion of blood. Future studies should investigate the role of compressibility, and in particular how fiber stress is altered when the material is allowed to compress. We clearly see stress effects related to the hydrostatic term in our model, and this will be investigated more closely in future studies.

Residual stresses are hypothesized to be important in stress estimation in soft biological tissue (Chuong and Fung 1986), and can be incorporated into the finite element model (Wang et al. 2014; Genet et al. 2015b). Because it has been shown in a previous study that residual stresses have little effects on ventricular function (Guccione et al. 2001), they were not considered in the present study. Nevertheless, the effect of including residual stresses in the estimation of fiber stress and contractility remains to be investigated in future studies

The late diastolic pressure-volume curve is fitted by estimating one material parameter, while fixing the remaining parameters to previously reported values (Asner et al. 2015). This is a limitation in our study, and future studies will be geared towards reducing the need for fixing these

model parameters by incorporating more clinical data or by revising the constitutive model. In particular, the incorporation of diastolic strains may be useful in more clearly defining material properties.

The simple estimation of unloaded configuration using only one iteration of the backward displacement method can be used with different initial material parameters and still recapitulate the end-diastolic volumes with different optimized material parameters. Several studies have jointly estimated the unloaded left-ventricular geometry and material parameters (Nikou et al. 2016; Finsberg et al. 2017; Asner et al. 2015), but estimation of the unloaded configuration with bi-ventricular geometries is not a well-posed problem, since buckling of the RV free wall might occur. More work on formulating well-posed algorithms for determining the unloaded configuration should be considered in future studies.

Finally, in this study we only considered three normal subjects, and in the future we would like to apply this framework to more individuals and use it to study larger cohorts as well as patients with cardiac pathology.

5 | CONCLUSION

Patient-specific simulations can now be assembled via adjoint-based data assimilation techniques, using no more than a few hours on a regular laptop. From these simulations we are able to extract information about myocardial contractility and fiber stress which shows low variability in the modeling choices that we make. Validation of these models should be the main objective in the years to come in order to translate cardiac computational modeling into clinical utility.

ACKNOWLEDGMENTS

This study was funded by Research Council of Norway: Center for Biomedical Computing at Simula Research Laboratory and Center for Cardiological Innovation at Oslo University Hospital. Computations were performed on the Abel supercomputing cluster at the University of Oslo via Notur project nn9249k. This study was also partially supported by Singapore Ministry of Health's National Medical Research Council (NMRC/OFIRG/0018/2016, Zhong), Goh Cardiovascular Research Award (Duke-NUS-GCR/2013/0009, Zhong), AHA SDG 17SDG33370110 (Lee) and R01-HL-134841 (Lee).

APPENDIX A: SENSITIVITY TO UNLOADED CONFIGURATION

The choice of initial material parameter a in the unloading algorithm will influence the estimated unloaded configuration. A softer material will result in a lower unloaded volume, hence the optimized material parameter will be softer to compensate for the greater volume increase from the reference to the end diastolic state. In the results presented in this study the value $a = 1.291$ kPa was chosen based on a parameter set used in (Asner et al. 2015).

To analyze the sensitivity of the results to the choice of material parameters used to unload the geometry, we unloaded the geometries using four different material parameters, i.e $a = 0.5, 1.0, 2.0$ and 4.0 kPa, and evaluated the corresponding model outputs. The resulting optimized material parameters, unloaded cavity volumes and value of the mismatch functional during the passive phase are shown in Table A1 .

For a more visual presentation, the LV and RV filling curves are presented to the left in Figure A1 for the different choices of unloaded configuration. From these results it is clear that even tough the different choices results in very different unloaded geometries, and passive material parameters, the mismatches between simulated and measured volumes are very small in all cases, except for $a = 0.5$ which hit the lower bound (of 0.05 kPa) set in the optimization.

Fiber stress and active strain are fairly consistent despite different unloaded geometries and material parameters (Figure A1). However, elevated fiber stresses can be seen during late systole for higher initial values of a. Furthermore, the magnitude of the active strain is increased in repose to stiffening of the material.

References

Alnæs, M., J. Blechta, J. Hake, A. Johansson, B. Kehlet, A. Logg, C. Richardson, J. Ring, M. E. Rognes, and G. N. Wells, 2015: The FEniCS Project Version 1.5. University Library Heidelberg. 00105.

TABLE A1 Optimized material parameters in kPa for different choice of unloaded configuration.

Patient ID	Initial a	a_{LV}	a_{RV}	$\mathcal{J}_{\mathrm{data}}$ (passive)	V_0^{LV}	V_0^{RV}
CASE1	0.5	0.05	0.321	0.000551	36.2	53.8
CASE1	1	0.165	0.699	7.13e-08	40.4	56.6
CASE1	2	0.64	1.49	1.81e-07	45.9	60.5
CASE1	4	1.92	2.91	2.46e-07	52.8	65.4
CASE2	0.5	0.05	0.29	0.000447	34.5	46.9
CASE2	1	0.168	0.736	8.06e-08	38.9	50.7
CASE2	2	0.642	1.79	3.27e-07	44.9	56.1
CASE2	4	2.03	4.01	9.79e-07	52.8	63.3
CASE3	0.5	0.05	1.03	0.00417	40.3	49.4
CASE3	1	0.0895	1.9	8.24e-07	44.8	52.8
CASE3	2	0.48	3.71	2.61e-06	50.8	57.5
CASE3	4	1.86	7.03	6.69e-06	59	63.5

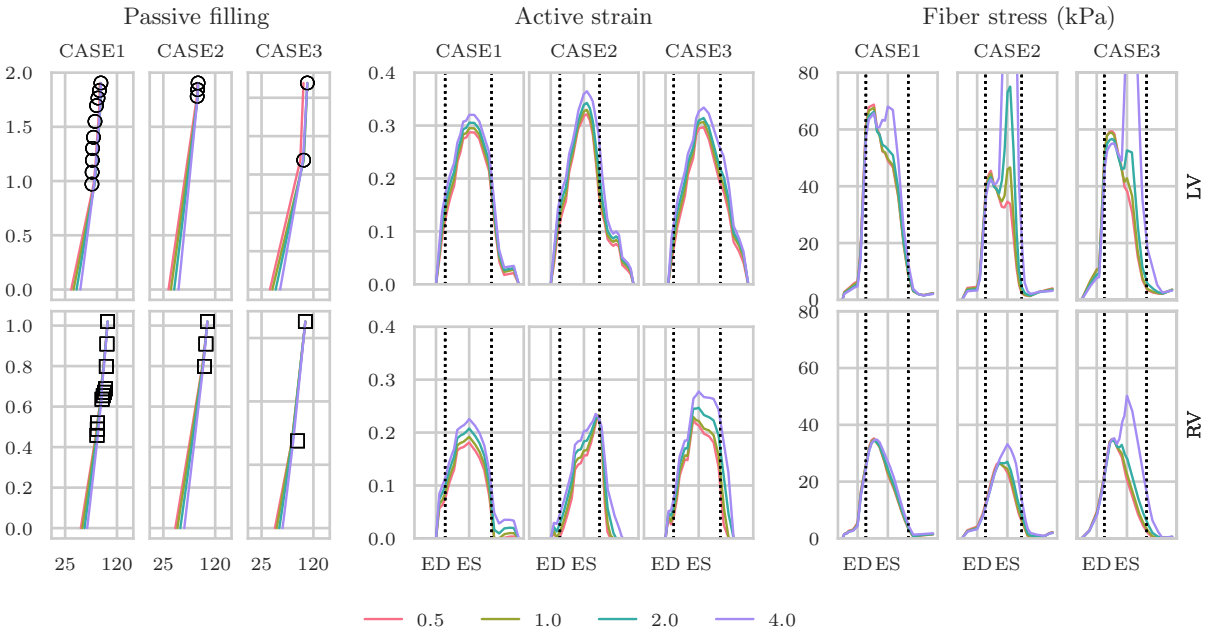

FIGURE A1 To the left we show the passive filling curves, with volume in ml on the $x-$axis and pressure in kPa on the $y-$axis with different unloaded volume resulting from different material parameters used to estimate the unloaded geometries. Middle and right panel show average time traces of estimated active strain and Cauchy fiber stress respectively for different choice of unloaded configuration. Top row shows the results in the left ventricle while bottom row shows the results in the right ventricle. Here the values $a = 0.5, 1.0, 2.0$ and 4.0 kPa are used to unload the ventricles.

Ambrosi, D., G. Arioli, F. Nobile, and A. Quarteroni, 2011: Electromechanical coupling in cardiac dynamics: the active strain approach. *SIAM Journal on Applied Mathematics*, **71**, no. 2, 605–621.

Asner, L., M. Hadjicharalambous, R. Chabiniok, D. Peresutti, E. Sammut, J. Wong, G. Carr-White, P. Chowienczyk, J. Lee, A. King, et al., 2015: Estimation of passive and active properties in the human heart using 3d tagged mri. *Biomechanics and modeling in mechanobiology*, 1–19.

Balaban, G., H. Finsberg, J. Sundnes, M. E. Rognes, H.-H. Odland, S. Ross, and S. T. Wall, 2016: High resolution data assimilation of cardiac mechanics applied to a dyssynchronous ventricle. *International Journal for Numerical Methods in Engineering*, **79**, no. 11, 1309–1331.

Bayer, J., R. Blake, G. Plank, and N. Trayanova, 2012: A novel rule-based algorithm for assigning myocardial fiber orientation to computational heart models. *Annals of biomedical engineering*, **40**, no. 10, 2243–2254.

Bols, J., J. Degroote, B. Trachet, B. Verhegghe, P. Segers, and J. Vierendeels, 2013: A computational method to assess the in vivo stresses and unloaded configuration of patient-specific blood vessels. *Journal of computational and Applied mathematics*, **246**, 10–17.

Brown, K. A. and R. V. Ditchey, 1988: Human right ventricular end-systolic pressure-volume relation defined by maximal elastance. *Circulation*, **78**, no. 1, 81–91.

Chabiniok, R., P. Moireau, P.-F. Lesault, A. Rahmouni, J.-F. Deux, and D. Chapelle, 2012: Estimation of tissue contractility from cardiac cine-mri using a biomechanical heart model. *Biomechanics and modeling in mechanobiology*, **11**, no. 5, 609–630.

Chabiniok, R., V. Y. Wang, M. Hadjicharalambous, L. Asner, J. Lee, M. Sermesant, E. Kuhl, A. A. Young, P. Moireau, M. P. Nash, et al., 2016: Multiphysics and multiscale modelling, data–model fusion and integration of organ physiology in the clinic: ventricular cardiac mechanics. *Interface focus*, **6**, no. 2, 20150083.

Chapelle, D. and K.-J. Bathe, 1993: The inf-sup test. *Computers & structures*, **47**, no. 4-5, 537–545.

Chapelle, D., M. Fragu, V. Mallet, and P. Moireau, 2013: Fundamental principles of data assimilation underlying the verdandi library: applications to biophysical model personalization within euheart. *Medical & biological engineering & computing*, **51**, no. 11, 1221–1233.

Chen, C.-H., M. Nakayama, E. Nevo, B. J. Fetics, W. L. Maughan, and D. A. Kass, 1998: Coupled systolic-ventricular and vascular stiffening with age. *Journal of the American College of Cardiology*, **32**, no. 5, 1221–1227.

Chuong, C.-J. and Y.-C. Fung, 1986: Residual stress in arteries. *Frontiers in biomechanics*, Springer, 117–129.

Claire, D., F. Hild, and S. Roux, 2004: A finite element formulation to identify damage fields: The equilibrium gap method. *Int. J. Numer. Methods Eng.*, **61**, no. 2, 189–208, doi:10.1002/nme.1057, 00000.

Delingette, H., F. Billet, K. C. Wong, M. Sermesant, K. Rhode, M. Ginks, C. A. Rinaldi, R. Razavi, and N. Ayache, 2012: Personalization of cardiac motion and contractility from images using variational data assimilation. *IEEE transactions on biomedical engineering*, **59**, no. 1, 20–24.

Farrell, P. E., D. A. Ham, S. W. Funke, and M. E. Rognes, 2013: Automated derivation of the adjoint of high-level transient finite element programs. *SIAM Journal on Scientific Computing*, **35**, no. 4, C369–C393.

Finsberg, H., G. Balaban, S. Ross, T. F. Håland, H. H. Odland, J. Sundnes, and S. Wall, 2017: Estimating cardiac contraction through high resolution data assimilation of a personalized mechanical model. *Journal of Computational Science*.

Gee, M. W., C. Förster, and W. Wall, 2010: A computational strategy for prestressing patient-specific biomechanical problems under finite deformation. *International Journal for Numerical Methods in Biomedical Engineering*, **26**, no. 1, 52–72.

Genet, M., L. C. Lee, L. Ge, G. Acevedo-Bolton, N. Jeung, A. J. Martin, N. Cambronero, A. J. Boyle, Y. Yeghiazarians, S. Kozerke, and J. M. Guccione, 2015a: A Novel Method for Quantifying Smooth Regional Variations in Myocardial Contractility Within an Infarcted Human Left Ventricle Based on Delay-Enhanced Magnetic Resonance Imaging. *J. Biomech. Eng.*, **137**, no. 8, doi:10.1115/1.4030667.

Genet, M., L. C. Lee, R. Nguyen, H. Haraldsson, G. Acevedo-Bolton, Z. Zhang, L. Ge, K. Ordovas, S. Kozerke, and J. M. Guccione, 2014: Distribution of normal human left ventricular myofiber stress at end diastole and end systole: a target for in silico design of heart failure treatments. *Journal of applied physiology*, **117**, no. 2, 142–152.

Genet, M., M. K. Rausch, L. C. Lee, S. Choy, X. Zhao, G. S. Kassab, S. Kozerke, J. M. Guccione, and E. Kuhl, 2015b: Heterogeneous growth-induced prestrain in the heart. *J. Biomech.*, **48**, no. 10, 2080–2089, doi:10.1016/j.jbiomech.2015.03.012.

Genet, M., C. T. Stoeck, C. von Deuster, L. C. Lee, J. M. Guccione, and S. Kozerke, 2016: Finite Element Digital Image Correlation for Cardiac Strain Analysis from 3D Whole-Heart Tagging. *24rd Annual Meeting of the International Society for Magnetic Resonance in Medicine (ISMRM2016)*.

Genet, M., C. T. Stoeck, C. Von Deuster, L. C. Lee, and S. Kozerke, 2017: Equilibrated warping: Finite element image correlation with finite strain equilibrium gap regularization. *Submitted*, 00000.

Geuzaine, C. and J.-F. Remacle, 2009: Gmsh: A 3-d finite element mesh generator with built-in pre-and post-processing facilities. *International Journal for Numerical Methods in Engineering*, **79**, no. 11, 1309–1331.

Gjerald, S., J. Hake, S. Pezzuto, J. Sundnes, and S. T. Wall, 2014: Patient–specific parameter estimation for a transversely isotropic active strain model of left ventricular mechanics. *Statistical Atlases and Computational Models of the Heart-Imaging and Modelling Challenges*, Springer, 93–104.

Göktepe, S., S. Acharya, J. Wong, and E. Kuhl, 2011: Computational modeling of passive myocardium. *International Journal for Numerical Methods in Biomedical Engineering*, **27**, no. 1, 1–12.

Govindjee, S. and P. A. Mihalic, 1996: Computational methods for inverse finite elastostatics. *Computer Methods in Applied Mechanics and Engineering*, **136**, no. 1, 47–57.

Grossman, W., D. Jones, and L. McLaurin, 1975: Wall stress and patterns of hypertrophy in the human left ventricle. *Journal of Clinical Investigation*, **56**, no. 1, 56.

Guccione, J. M., S. M. Moonly, A. W. Wallace, and M. B. Ratcliffe, 2001: Residual stress produced by ventricular volume reduction surgery has little effect on ventricular function and mechanics: a finite element model study. *The Journal of thoracic and cardiovascular surgery*, **122**, no. 3, 592–599.

Guccione, J. M., A. Salahieh, S. M. Moonly, J. Kortsmit, A. W. Wallace, and M. B. Ratcliffe, 2003: Myosplint decreases wall stress without depressing function in the failing heart: a finite element model study. *The Annals of thoracic surgery*, **76**, no. 4, 1171–1180.

Ho, S. and P. Nihoyannopoulos, 2006: Anatomy, echocardiography, and normal right ventricular dimensions. *Heart*, **92**, no. suppl 1, i2–i13.

Holzapfel, G. A. and R. W. Ogden, 2009: Constitutive modelling of passive myocardium: a structurally based framework for material characterization. *Philosophical Transactions of the Royal Society of London A: Mathematical, Physical and Engineering Sciences*, **367**, no. 1902, 3445–3475.

Hood, P. and C. Taylor, 1974: Navier-stokes equations using mixed interpolation. *Finite element methods in flow problems*, 121–132.

Huisman, R. M., G. Elzinga, N. Westerhof, and P. Sipkema, 1980: Measurement of left ventricular wall stress. *Cardiovascular research*, **14**, no. 3, 142–153.

Hunter, P., A. McCulloch, and H. Ter Keurs, 1998: Modelling the mechanical properties of cardiac muscle. *Progress in biophysics and molecular biology*, **69**, no. 2, 289–331.

Kelly, R. P., C. T. Ting, T. M. Yang, C. P. Liu, W. L. Maughan, M. S. Chang, and D. A. Kass, 1992: Effective arterial elastance as index of arterial vascular load in humans. *Circulation*, **86**, no. 2, 513–521, doi:10.1161/01.CIR.86.2.513.

Kraft, D. et al., 1988: *A software package for sequential quadratic programming*. DFVLR Obersfaffeuhofen, Germany.

Krishnamurthy, A., C. T. Villongco, J. Chuang, L. R. Frank, V. Nigam, E. Belezzuoli, P. Stark, D. E. Krummen, S. Narayan, J. H. Omens, A. D. McCulloch, and R. C. Kerckhoffs, 2013: Patient-Specific Models of Cardiac Biomechanics. *Journal of computational physics*, **244**, 4–21, doi:10.1016/j.jcp.2012.09.015.
URL http://www.ncbi.nlm.nih.gov/pubmed/23729839

Kroon, W., T. Delhaas, P. Bovendeerd, and T. Arts, 2009: Computational analysis of the myocardial structure: Adaptation of cardiac myofiber orientations through deformation. *Medical image analysis*, **13**, no. 2, 346–353.

Lamata, P., R. Casero, V. Carapella, S. A. Niederer, M. J. Bishop, J. E. Schneider, P. Kohl, and V. Grau, 2014: Images as drivers of progress in cardiac computational modelling. *Progress in biophysics and molecular biology*, **115**, no. 2, 198–212.

Lee, L. C., M. Genet, A. B. Dang, L. Ge, J. M. Guccione, and M. B. Ratcliffe, 2014: Applications of computational modeling in cardiac surgery. *J. Card. Surg.*, **29**, no. 3, 293–302, doi:10.1111/jocs.12332.

Lee, L. C., S. T. Wall, D. Klepach, L. Ge, Z. Zhang, R. J. Lee, A. Hinson, J. H. Gorman, R. C. Gorman, and J. M. Guccione, 2013: Algisyl-lvr^{TM} with coronary artery bypass grafting reduces left ventricular wall stress and improves function in the failing human heart. *International journal of cardiology*, **168**, no. 3, 2022–2028.

LeGrice, I. J., B. Smaill, L. Chai, S. Edgar, J. Gavin, and P. J. Hunter, 1995: Laminar structure of the heart: ventricular myocyte arrangement and connective tissue architecture in the dog. *American Journal of Physiology-Heart and Circulatory Physiology*, **269**, no. 2, H571–H582.

Li, X. S. and J. W. Demmel, 2003: Superlu_dist: A scalable distributed-memory sparse direct solver for unsymmetric linear systems. *ACM Transactions on Mathematical Software (TOMS)*, **29**, no. 2, 110–140.

Lin, D. and F. Yin, 1998: A multiaxial constitutive law for iviammalian left ventricular myocardium in steady-state barium contracture or tetanus. *Journal of Biomechanical Engineering*, **120**, no. 4.

Logg, A., K.-A. Mardal, and G. Wells, 2012: *Automated solution of differential equations by the finite element method: The fenics book*.

Mansi, T., X. Pennec, M. Sermesant, H. Delingette, and N. Ayache, 2011: iLogDemons: A Demons-Based Registration Algorithm for Tracking Incompressible Elastic Biological Tissues. *Int. J. Comput. Vis.*, **92**, no. 1, 92–111, doi:10.1007/s11263-010-0405-z, 00101.

Marchesseau, S., H. Delingette, M. Sermesant, R. Cabrera-Lozoya, C. Tobon-Gomez, P. Moireau, R. F. i Ventura, K. Lekadir, A. Hernandez, M. Garreau, et al., 2013: Personalization of a cardiac electromechanical model using reduced order unscented kalman filtering from regional volumes. *Medical image analysis*, **17**, no. 7, 816–829.

Marler, R. T. and J. S. Arora, 2004: Survey of multi-objective optimization methods for engineering. *Structural and multidisciplinary optimization*, **26**, no. 6, 369–395.

Moireau, P. and D. Chapelle, 2011: Reduced-order unscented kalman filtering with application to parameter identification in large-dimensional systems. *ESAIM: Control, Optimisation and Calculus of Variations*, **17**, no. 2, 380–405.

Nair, A. U., D. G. Taggart, and F. J. Vetter, 2007: Optimizing cardiac material parameters with a genetic algorithm. *Journal of biomechanics*, **40**, no. 7, 1646–1650.

Nikou, A., S. M. Dorsey, J. R. McGarvey, J. H. Gorman III, J. A. Burdick, J. J. Pilla, R. C. Gorman, and J. F. Wenk, 2016: Effects of using the unloaded configuration in predicting the in vivo diastolic properties of the heart. *Computer methods in biomechanics and biomedical engineering*, **19**, no. 16, 1714–1720.

Pope, A. J., G. B. Sands, B. H. Smaill, and I. J. LeGrice, 2008: Three-dimensional transmural organization of perimysial collagen in the heart. *American Journal of Physiology-Heart and Circulatory Physiology*, **295**, no. 3, H1243–H1252.

Rausch, M. K., M. Genet, and J. D. Humphrey, 2017: An augmented iterative method for identifying a stress-free reference configuration in image-based biomechanical modeling. *J. Biomech.*, **58**, 227–231, doi:10.1016/j.jbiomech.2017.04.021, 00000.

Redington, A. N., H. H. Gray, M. E. Hodson, M. L. Rigby, and P. J. Oldershaw, 1988: Characterisation of the normal right ventricular pressure-volume relation by biplane angiography and simultaneous micromanometer pressure measurements. *Br Heart J*, **59**, no. 1, 23–30, doi:10.1136/hrt.59.1.23.

Sagawa, K., H. Suga, A. A. Shoukas, and K. M. Bakalar, 1977: End-systolic pressure/volume ratio: a new index of ventricular contractility. *The American journal of cardiology*, **40**, no. 5, 748–753.

Scardulla, F., A. Rinaudo, S. Pasta, and C. Scardulla, 2016: Evaluation of ventricular wall stress and cardiac function in patients with dilated cardiomyopathy. *Proceedings of the Institution of Mechanical Engineers, Part H: Journal of Engineering in Medicine*, **230**, no. 1, 71–74.

Sellier, M., 2011: An iterative method for the inverse elasto-static problem. *J. Fluids Struct.*, **27**, no. 8, 1461–1470, doi:10.1016/j.jfluidstructs.2011.08.002.

Sermesant, M., R. Chabiniok, P. Chinchapatnam, T. Mansi, F. Billet, P. Moireau, J.-M. Peyrat, K. Wong, J. Relan, K. Rhode, et al., 2012: Patient-specific electromechanical models of the heart for the prediction of pacing acute effects in crt: a preliminary clinical validation. *Medical image analysis*, **16**, no. 1, 201–215.

Sermesant, M., P. Moireau, O. Camara, J. Sainte-Marie, R. Andriantsimiavona, R. Cimrman, D. L. Hill, D. Chapelle, and R. Razavi, 2006: Cardiac function estimation from mri using a heart model and data assimilation: advances and difficulties. *Medical Image Analysis*, **10**, no. 4, 642–656.

Streeter, D. D., H. M. Spotnitz, D. P. Patel, J. Ross, and E. H. Sonnenblick, 1969: Fiber orientation in the canine left ventricle during diastole and systole. *Circulation research*, **24**, no. 3, 339–347.

Sun, K., N. Stander, C.-S. Jhun, Z. Zhang, T. Suzuki, G.-Y. Wang, M. Saeed, A. W. Wallace, E. E. Tseng, A. J. Baker, et al., 2009: A computationally efficient formal optimization of regional myocardial contractility in a sheep with left ventricular aneurysm. *Journal of biomechanical engineering*, **131**, no. 11, 111001.

Sundnes, J., S. Wall, H. Osnes, T. Thorvaldsen, and A. D. McCulloch, 2014: Improved discretisation and linearisation of active tension in strongly coupled cardiac electro-mechanics simulations. *Computer methods in biomechanics and biomedical engineering*, **17**, no. 6, 604–615.

Toussaint, N., C. T. Stoeck, T. Schaeffter, S. Kozerke, M. Sermesant, and P. G. Batchelor, 2013: In vivo human cardiac fibre architecture estimation using shape-based diffusion tensor processing. *Medical image analysis*, **17**, no. 8, 1243–1255.

Townsend, D., 2008: Multimodality imaging of structure and function. *Physics in medicine and biology*, **53**, no. 4, R1.

Veress, A. I., G. T. Gullberg, and J. A. Weiss, 2005: Measurement of Strain in the Left Ventricle during Diastole with cine-MRI and Deformable Image Registration. *J. Biomech. Eng.*, **127**, no. 7, 1195, doi:10.1115/1.2073677.

Wall, S. T., J. C. Walker, K. E. Healy, M. B. Ratcliffe, and J. M. Guccione, 2006: Theoretical impact of the injection of material into the myocardium: a finite element model simulation. *Circulation*, **114 24**, 2627–35.

Wang, H., X. Luo, H. Gao, R. Ogden, B. Griffith, C. Berry, and T. Wang, 2014: A modified holzapfel-ogden law for a residually stressed finite strain model of the human left ventricle in diastole. *Biomechanics and modeling in mechanobiology*, **13**, no. 1, 99–113.

Wang, V., P. Nielsen, and M. Nash, 2015: Image-based predictive modeling of heart mechanics. *Annual review of biomedical engineering*, **17**, 351–383.

Wang, V. Y., H. Lam, D. B. Ennis, B. R. Cowan, A. A. Young, and M. P. Nash, 2009: Modelling passive diastolic mechanics with quantitative mri of cardiac structure and function. *Medical image analysis*, **13**, no. 5, 773–784.

Weiss, J. A., B. N. Maker, and S. Govindjee, 1996: Finite element implementation of incompressible, transversely isotropic hyperelasticity. *Computer methods in applied mechanics and engineering*, **135**, no. 1-2, 107–128.

Xi, C., C. Latnie, X. Zhao, J. Le Tan, S. T. Wall, M. Genet, L. Zhong, and L. C. Lee, 2016: Patient-specific computational analysis of ventricular mechanics in pulmonary arterial hypertension. *Journal of biomechanical engineering*, **138**, no. 11, 111001.

Xi, J., P. Lamata, S. Niederer, S. Land, W. Shi, X. Zhuang, S. Ourselin, S. G. Duckett, A. K. Shetty, C. A. Rinaldi, et al., 2013: The estimation of patient-specific cardiac diastolic functions from clinical measurements. *Medical image analysis*, **17**, no. 2, 133–146.

Yin, F., 1981: Ventricular wall stress. *Circulation Research*, **49**, no. 4, 829–842.

Zhang, Z., A. Tendulkar, K. Sun, D. A. Saloner, A. W. Wallace, L. Ge, J. M. Guccione, and M. B. Ratcliffe, 2011: Comparison of the young-laplace law and finite element based calculation of ventricular wall stress: implications for postinfarct and surgical ventricular remodeling. *The Annals of thoracic surgery*, **91**, no. 1, 150–156.

AUTHOR BIOGRAPHY

Henrik Finsberg. Henrik Finsberg graduated in 2014 after finishing a joint master degree in Applied and Engineering Mathematics at NTNU in Trondheim and DTU in Copenhagen. He is currently pursuing a Ph.D. at Simula Research Laboratory in the Center for Cardiological Innovation working with patient specific modeling of the heart. Areas of interests includes mathematical modeling, image analysis, visualization and geometric modeling.

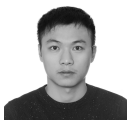

Ce Xi. Ce Xi obtained his bachelor's degree in Naval Architecture and Ocean Engineering at Huazhong University of Science and Technology, China in 2014. Presently, he is pursuing a Ph.D. degree in Mechanical Engineering at Michigan State University, USA. His research interests include patient-specific computational analysis of ventricular mechanics and microstructural modeling of cardiac tissues.

Ju Le Tan. Ju Le Tan is the Senior Consultant Cardiologist specialising in Adult Congenital Heart Disease and Echocardiography at the National Heart Centre Singapore. She has gone for training in Adult Congenital Heart Disease at the Royal Brompton Hospital in London in 2003 to 2005. Her main interest is the care of adults with congenital heart disease, management of cardiac disease in pregnancy and pulmonary hypertension. She is a part-time Senior Lecturer at the National University of Singapore and Singapore Polytechnic.

Liang Zhong. Liang Zhong is Principal Investigator and directing cardiovascular bioengineering theme in National Heart Centre Singapore and Assistant Professor at the Duke National University of Singapore. He received the Ph.D. degree from Nanyang Technological University in 2005. His research interests include advanced cardiac imaging, cardiovascular biomechanics, computational fluid dynamics, and coronary circulation in health and disease.

Martin Genet. Martin Genet obtained his PhD from *École Normale Supérieure*, Cachan, France, in 2010, and was then a postdoctoral fellow at the Lawrence Berkeley National Laboratory, California, USA, from 2010 to 2012. In 2012 he obtained a Marie-Curie International Outgoing fellowship to work on patient-specific cardiac modeling, at the University of California at San Francisco, USA, and Stanford University, Palo Alto, USA, from 2012 to 2014, and at the Swiss Federal Institute of Technology (ETH), Zurich, Switzerland, from 2014 to 2015. Since 2015 he is an Assistant Professor at *École Polytechnique*, Palaiseau, France, where he works on mechanical modeling and simulation, with data interaction, of soft tissues.

Joakim Sundnes. Joakim Sundnes is a Senior Research Scientist at Simula Research Laboratory and an Associate Professor at University of Oslo. He holds a PhD in Scientific Computing from the University of Oslo, and his main research interests are computational modeling of cardiac electrophysiology and mechanics.

Lik Chuan Lee. Lik Chuan Lee is an Assistant Professor in Mechanical Engineering at Michigan State University. He received his Ph.D in Mechanical Engineering from the University of California, Berkeley. His main research interests are in computational modeling of soft tissues with a focus on cardiac electromechanics .

Samuel Wall Samuel Wall is the head of the Cardiac Modeling (CaMo) group at Simula Research Laboratory and is an Associate Professor at the Norwegian University of Life Science. He received his Ph.D. in Bioengineering jointly from the University of California, Berkeley and the University of California, San Francisco and his work is focused on ventricular modeling of mechanical and electromechanical function of the heart.